CCS CHINESE CHEMICAL SOCIETY

ROYAL SOCIETY OF CHEMISTRY

Check for updates

Highly efficient electrochemical CO_2 reduction over crystalline–amorphous In_2O_3–CeO_x heterostructures†

Cuifeng Wang, Zhaohui Wu, Guihao Liu, Sha Bai, Lin Guo, Lei He [ID] * and Yu-Fei Song [ID] *

The electrochemical reduction reaction of CO_2 (CO_2RR) to fuels and chemicals is a promising approach to consume greenhouse gases and mitigate the dependence on fossil fuels. Herein, we synthesized an effective crystalline–amorphous In_2O_3–CeO_x heterostructure, which exhibited high catalytic performance for CO_2-to-formate conversion. The maximum faradaic efficiency (FE) of 94.8% was achieved, and above 90% FE can be maintained in a wide potential range from −0.8 to −1.2 V *vs.* RHE. Detailed studies showed that In_2O_3 functioned as the active site for CO_2 activation and formate formation, and the amorphous CeO_x was beneficial for the electron transfer, leading to the electronic structure reconfiguration of In_2O_3. Hence, the In_2O_3–CeO_x heterostructure enhanced the adsorption of *OCHO intermediates and lowered the energy barrier forming *HCOOH from *OCHO.

Introduction

The electrochemical reduction reaction of CO_2 (CO_2RR) into value-added chemicals and fuels is a promising approach to consume excess industrial CO_2 emissions and address the current ongoing consumption of non-renewable fossil fuels.[1–4] Nevertheless, there are still problems restricting the practical application of the CO_2RR. For example, CO_2 gas molecules are thermodynamically stable, and the complexity of the reaction pathway as well as the competitive hydrogen evolution reaction (HER) leads to diverse products and low selectivity. Considering the cost of electricity and the product's market price, the two-electron transfer products formate and CO are the most promising target products among the numerous CO_2 reduction products.[5] Formate is one of the fundamental starting materials for industrial production, which is widely used in the fields of pesticides, dyes, medicine, rubber and tanning industries.[6] As such, efficient catalysts need to be developed to lower the energy barrier and improve the selectivity for converting CO_2 to formate.

The p-block metals such as In, Bi, Pb, and Sn are efficient catalysts for CO_2 electroreduction due to their high overpotential for the HER.[7–10] Among them, low-toxicity and environmentally friendly In-based materials show high selectivity to formate.[11]

Various strategies on In-based catalysts have been proposed such as morphology design,[12] defect engineering,[13] doping,[14] and alloying[15] to reinforce the catalytic activities. Although these strategies are ingenious in design, they still suffer from cumbersome synthetic procedures, and the electrochemical performance still needs to be further improved. As such, the development of novel In-based catalysts is promising for electroreduction of CO_2 to formate.

Constructing heterostructures is an effective strategy to enhance the electrocatalytic performance due to their efficient charge transfer at the interface and the sufficiently exposed catalytically active sites.[16–18] In particular, heterostructures can direct high selectivity toward a specific product in complicated CO_2RR reaction routes *via* adjusting the binding strength with key intermediates.[19,20] CeO_2-based materials possess unique transformation characteristics between Ce^{3+} and Ce^{4+} states, which are beneficial for the gain and loss of electrons,[21] and have been proved to significantly strengthen the adsorption and promote the activation of CO_2 molecules. These properties make CeO_2 suitable for constructing heterostructures to enhance the CO_2 conversion process. For example, Bao *et al.*[22] have demonstrated that the CO_2RR can be significantly improved by the interface of Au–CeO_x heterostructures. Gong *et al.*[23] have revealed that high Ce^{3+} concentration is beneficial for CO_2 activation. Notably, in comparison with their crystalline–crystalline counterparts, crystalline–amorphous heterostructures can inherit the merits of amorphous structures, such as abundant active sites and defects, high flexibility, and better corrosion resistance.[24,25] Therefore, rational design of crystalline–amorphous heterostructures is an effective method to achieve the purpose of improving CO_2RR performance.

State Key Laboratory of Chemical Resource Engineering, Beijing University of Chemical Technology, Beijing 100029, P. R. China. E-mail: helei@mail.buct.edu.cn, songyf@mail.buct.edu.cn; Fax: +86 10 64431832; Tel: +86 10 64431832

†Electronic supplementary information (ESI) available. See DOI: https://doi.org/10.1039/d2qi01646j

5926 | *Inorg. Chem. Front.*, 2022, **9**, 5926–5931

This journal is © the Partner Organisations 2022

Herein, crystalline–amorphous In_2O_3–CeO_x heterostructures were fabricated for the first time and were used as an electrocatalyst for the CO_2RR. It was discovered that the maximum faradaic efficiency (FE) can reach 94.8% at −0.9 V *vs.* RHE over In_2O_3–CeO_x, which was obviously more efficient than those of a pure In_2O_3 catalyst and a crystalline–crystalline In_2O_3–CeO_2 heterostructure. The improved performance of the In_2O_3–CeO_x catalyst was attributed to the electronic reconfiguration of indium by strengthened electron transfer between In_2O_3 and amorphous CeO_x, which significantly enhanced the adsorption of *OCHO intermediates and lowered the energy barrier of *OCHO → *HCOOH, leading to the high activity and selectivity for the CO_2RR to formate.

Results and discussion

The In_2O_3–CeO_x catalyst was synthesized *via* two steps (Fig. S1a†). Firstly, an aqueous solution containing indium nitrate, sodium carbonate and as-prepared CeO_x was stirred to form an $In(OH)_3$–CeO_x precipitate for one hour at room temperature. Secondly, the precursor $In(OH)_3$–CeO_x was annealed under an Ar/H_2 flow for one hour to obtain the In_2O_3–CeO_x catalyst. The structures of the samples (*e.g.*, In_2O_3–CeO_x, In_2O_3–CeO_2, the individual CeO_x, CeO_2 and In_2O_3) were determined using X-ray diffraction (XRD) patterns. As shown in Fig. 1a, no obvious peak was observed for CeO_x, suggesting that the amorphous structure was successfully achieved. In addition, no obvious peak of In_2O_3 was observed in the In_2O_3–CeO_x sample, which was caused by the small particle size and uniform dispersion of In_2O_3. In contrast, CeO_2 displayed the characteristic peaks of the crystal structure, which were consistent with those reported in the literature (Fig. 1b).[26] The

peaks of In_2O_3–CeO_2 matched well with the standard patterns of CeO_2 and In_2O_3, as shown in Fig. 1b. The high-resolution transmission electron microscopy (HR-TEM) images showed the crystalline–amorphous heterostructure interface of In_2O_3–CeO_x and crystalline–crystalline heterostructure interface of In_2O_3–CeO_2 (Fig. 1c–f). As shown in Fig. 1d, the lattice fringe of In_2O_3–CeO_x could be assigned to the (222) plane of In_2O_3 while the amorphous CeO_x did not show any lattice stripes. In contrast, the HR-TEM image of In_2O_3–CeO_2 clearly presented the lattice fringes for the (222) facet of In_2O_3 and (111) facet of CeO_2 (Fig. 1f). Furthermore, energy dispersive X-ray spectroscopy (EDX) elemental mapping of the samples showed that In, Ce, and O were evenly distributed (Fig. 1g–j and S2†), confirming the successful preparation of In_2O_3–CeO_x and In_2O_3–CeO_2 heterostructures.

X-ray photoelectron spectroscopy (XPS) was utilized to investigate the electronic properties and chemical compositions of the samples. The Ce 3d XPS spectra of CeO_x showed the presence of both Ce^{4+} and Ce^{3+} peaks (Fig. 2a), where Ce^{3+} included one pair of peaks (V and V′), whilst Ce^{4+} had two pairs of peaks (U_1, U_2, $U′_1$, and $U′_2$). Notably, the proportion of Ce^{3+} in In_2O_3–CeO_x was increased to 48.3% (Fig. 2b) compared to the individual CeO_x (43.2%). In contrast, the proportion of Ce^{3+} in In_2O_3–CeO_2 showed no obvious variation compared to that in CeO_2 (Fig. S3a and b†). Additionally, the In 3d spectra of In_2O_3 showed two peaks at 451.7 (In $3d_{3/2}$) and 444.2 eV (In $3d_{5/2}$), while the binding energy of In 3d in In_2O_3–CeO_x shifted positively about 1 eV compared to that of In_2O_3 (Fig. 2c). The results demonstrated the strong interaction between In_2O_3 and CeO_x, and electrons transferred from the crystalline In_2O_3 to amorphous CeO_x, which led to an increase in the proportion of Ce^{3+} in In_2O_3–CeO_x. Moreover, the linear sweep voltammetry (LSV) curves of In_2O_3 showed an obvious reduction peak at

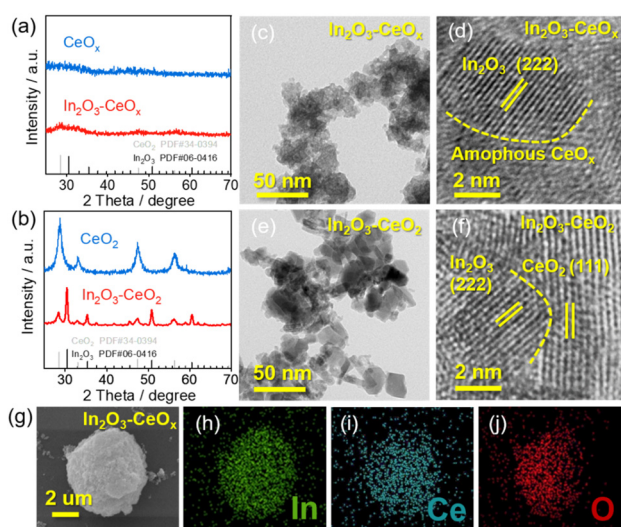**Fig. 1** (a) XRD patterns of CeO_x and In_2O_3–CeO_x, (b) XRD patterns of CeO_2 and In_2O_3–CeO_2, (c and d) HR-TEM image of In_2O_3–CeO_x and (e and f) HR-TEM image of In_2O_3–CeO_2. (g–j) The corresponding EDX elemental mapping of $In_2O_3CeO_x$.
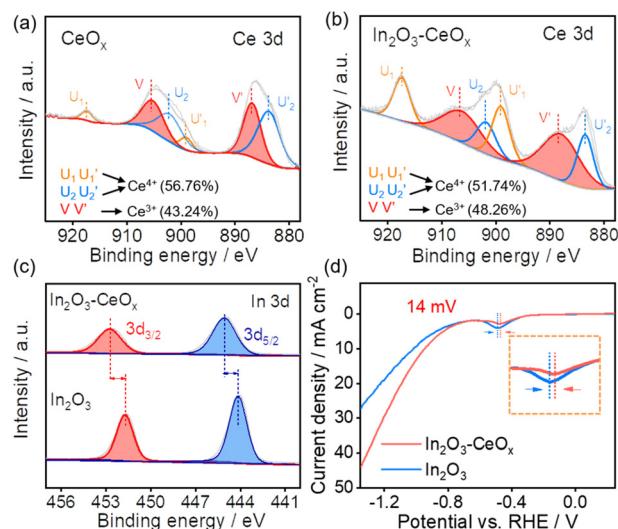
Fig. 2 Ce 3d XPS spectra of (a) CeO_x and (b) In_2O_3–CeO_x; (c) In 3d XPS spectra of In_2O_3–CeO_x and In_2O_3; and (d) LSVs of In_2O_3 and In_2O_3–CeO_x in CO_2-saturated 0.5 M $KHCO_3$ at a scan rate of 50 mV s^{-1}.

−0.487 V (*vs.* RHE), corresponding to a typical In^{3+}/In^0 reduction peak (Fig. S4†).[27]

It should be noted that the reduction peak potential of In_2O_3–CeO_x positively shifted by 14 mV (appearing at −0.473 V) (Fig. 2d). The lower reduction potential of In_2O_3–CeO_x meant an enhanced electrochemical redox activity.[28] In contrast, no obvious change in the reduction peak potential was detected for In_2O_3–CeO_2 compared to that of In_2O_3 (Fig. S3c†). This result was consistent with the XPS data, revealing that the crystalline–amorphous heterostructure of In_2O_3–CeO_x led to stronger interactions between its individual components.

The electrocatalytic CO_2RR performances of In_2O_3, In_2O_3–CeO_x, and In_2O_3–CeO_2 were tested in a three-electrode system, with CO_2 saturated 0.1 M $KHCO_3$ as an electrolyte. Linear sweep voltammetry (LSV) curves were obtained at a scan rate of 50 mV s^{-1} between −1.38 V and −0.62 V (*vs.* RHE, all potentials used were *vs.* RHE unless otherwise stated). As depicted by the linear sweep voltammetry (LSV) curves of all catalysts (Fig. 3a and S5†), significantly higher current density was observed in CO_2 than that under an Ar atmosphere, indicating that the CO_2 reduction reaction occurred over these catalysts. Meanwhile, the current density of In_2O_3–CeO_x was larger than those of In_2O_3–CeO_2 and In_2O_3 in a CO_2-saturated electrolyte, indicating that a crystalline–amorphous In_2O_3–CeO_x heterostructure shows the best CO_2RR performance.

To further analyze the electroreduction products, controlled potential electrolysis of CO_2 was performed at a constant working potential ranging from −0.6 V to −1.3 V. The gaseous and liquid products were quantified by gas chromatography (GC) and nuclear magnetic resonance (NMR) spectroscopy, respectively. For In_2O_3, In_2O_3–CeO_2 and In_2O_3–CeO_x catalysts, CO and H_2 were detected as gas products, and formate was the unique liquid product (Fig. S6†). The formate faradaic efficiency ($FE_{formate}$) of the three catalysts all exhibited a volcanic-like pattern over the range of applied operating potentials, among which, the In_2O_3–CeO_x electrode exhibited higher selectivity toward formate against H_2 and CO (Fig. 3b and c). More remarkably, the $FE_{formate}$ on the In_2O_3–CeO_x electrode remained above 90% over a wide electrochemical window from −0.8 V to −1.2 V. The maximum $FE_{formate}$ reached 94.8% with a current density of 7 mA cm^{-2} at −0.9 V (Fig. 3c). By comparison, the maximum $FE_{formate}$ for In_2O_3–CeO_2 and In_2O_3 electrodes was only 74.2% and 73.6%, respectively, under −1.0 V (Fig. S7a and b†). The optimal electrolysis potential of In_2O_3–CeO_x was more positive than that of In_2O_3 and In_2O_3–CeO_2, which suggested that lower electrical energy was required to cross the energy barrier and realize the CO_2RR by the In_2O_3–CeO_x catalyst. Notably, H_2 was the only product of the individual CeO_x and CeO_2 (Fig. S7c and d†), indicating that the amorphous and crystalline ceria contributed to the formate formation *via* functions rather than being the catalyst.

The stability of In_2O_3–CeO_x was tested by continuous electrolysis at −0.9 V. As shown in Fig. 3d, no evident decay of current density and $FE_{formate}$ was observed after 20 h-electrolysis, demonstrating the good stability of the prepared In_2O_3–CeO_x electrode. Moreover, the LSV curves before and after long-term test showed no obvious difference (Fig. S8†), which further manifested the good stability of In_2O_3–CeO_x. After the test, the element mapping of In_2O_3–CeO_x showed that In, Ce, and O were uniformly distributed (Fig. S9†). In addition, the HRTEM image of In_2O_3–CeO_x after electrolysis still showed the amorphous morphology of CeO_x and the (222) plane of In_2O_3 (Fig. S9a and b†), indicating that the crystalline–amorphous heterostructure of In_2O_3–CeO_x can be retained during the electrolytic process.

To gain a deeper understanding of the kinetics of CO_2 electroreduction, we fitted the overpotentials of the three catalysts as a function of the bias current density for formate production to obtain the corresponding Tafel slopes (Fig. 4a). In_2O_3–CeO_x presented a smaller calculated Tafel slope (176 mV dec^{-1}) compared to In_2O_3–CeO_2 (186 mV dec^{-1}) and pure In_2O_3 (375 mV dec^{-1}). The smallest Tafel slope of In_2O_3–CeO_x suggested the largest increment in the CO_2 reduction rate with the increasing overpotential. The electron transfer properties were further investigated by an electrochemical impedance spectroscopy (EIS) test. As shown in Fig. 4b, In_2O_3–CeO_x showed smaller charge transfer resistance (R_{ct}) compared to In_2O_3–CeO_2 and In_2O_3. The results suggested that the crystalline–amorphous heterostructure rendered faster charge transfer than the bare In_2O_3 and crystalline–crystalline heterostructure, and the interaction of electrochemically active In_2O_3 with the amorphous CeO_x led to a more efficient electron transfer. The electrochemically active surface area (ECSA) was evaluated by the electrochemical double layer capacitance (C_{dl}) due to their positive proportion relationship (Fig. 4c).[2,29,30] The ECSA of In_2O_3–CeO_x (13.75 cm^{-2}) was higher than those of In_2O_3–CeO_2 (11.50 cm^{-2}) and In_2O_3 (9.50 cm^{-2}), which can promote the electrocatalytic performance. In addition, the
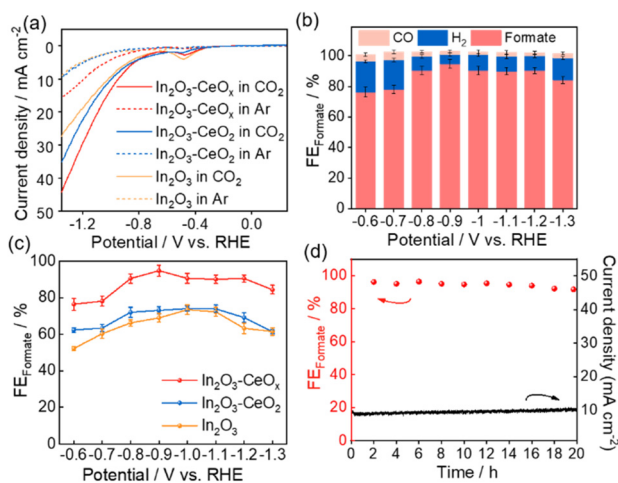

Fig. 3 CO_2 electroreduction in a 0.5 M $KHCO_3$ electrolyte. (a) LSV curves of In_2O_3–CeO_x, In_2O_3–CeO_2 and In_2O_3 electrodes in a CO_2-saturated electrolyte. (b) The $FE_{formate}$, FE_{CO} and FE_{H_2} of In_2O_3–CeO_x at different applied potentials, respectively. (c) $FE_{formate}$ of In_2O_3–CeO_x, In_2O_3–CeO_2 and In_2O_3 at different applied potentials, respectively. (d) Long-term stability of the CO_2 electroreduction for In_2O_3–CeO_x at −0.9 V (*vs.* RHE).

5928 | *Inorg. Chem. Front.*, 2022, **9**, 5926–5931
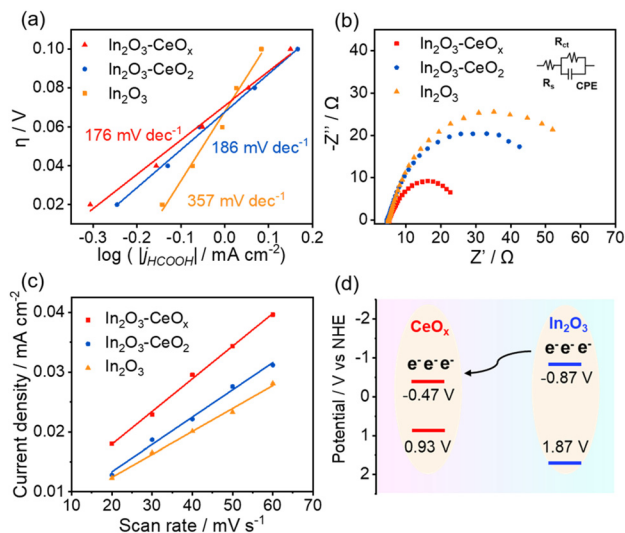
This journal is © the Partner Organisations 2022

Fig. 4 Advantages of In_2O_3–CeO_x for CO_2 reduction. (a) Tafel plots, (b) Nyquist plots (inset: equivalent circuit), (c) linear fitting of double-layer capacitive currents *versus* scan rates to estimate the ECSA of In_2O_3–CeO_x, In_2O_3–CeO_2 and In_2O_3, and (d) schematic illustration of the charge transfer in In_2O_3–CeO_x.
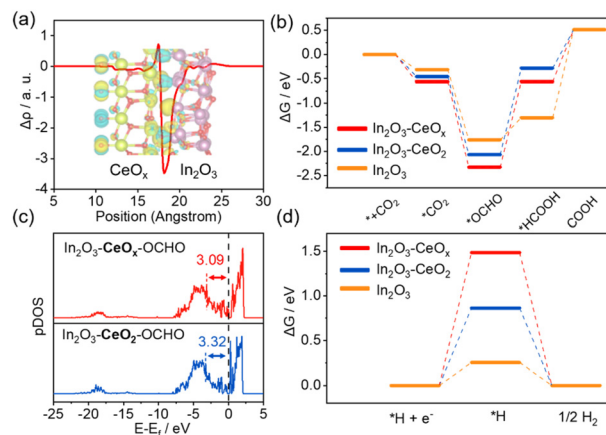

Fig. 5 DFT calculations. (a) Charge density difference and charge displacement curves of In_2O_3–CeO_x; purple, yellow, and red spheres represent In, Ce, and O atoms, respectively. (b) Gibbs free-energy diagrams of CO_2-to-formate. (c) In-5p p-DOS of In_2O_3–CeO_x and In_2O_3–CeO_2 after adsorbing *OCHO. (d) Gibbs free-energy diagrams of the HER.

partial current density of formate was normalized by the ECSA (Fig. S11†).[2] Similar to the geometric current density, the normalized current density of In_2O_3–CeO_x was the highest among the three samples. The rough surface of the CeO_x substrate promoted the adsorption and dispersion of In_2O_3, thereby increasing the active surface area. Furthermore, to verify the phenomenon of electron transfer between In_2O_3 and CeO_x in In_2O_3–CeO_x, we performed Mott–Schottky and valence band XPS experiments (Fig. S12†). As shown in Fig. 4d, the flat band potentials of In_2O_3 and CeO_x were located at −0.87 V and −0.47 V (*vs.* NHE), respectively. Such a band alignment can effectively facilitate the interfacial electrons transferring from the key component In_2O_3 to CeO_x. However, the flat band and valence band potentials of CeO_2 and In_2O_3 were not significantly different (Fig. S13†), and thus electron transfer hardly occurred between CeO_2 and In_2O_3.

Density functional theory (DFT) calculations were carried out to shed light on the origin of the enhanced activity of In_2O_3–CeO_x for the CO_2RR (Fig. S14–S16†). The charge density difference and charge displacement curves of In_2O_3–CeO_x and In_2O_3–CeO_2 were obtained to study the transfer of electrons.[31–33] As shown in Fig. 5a, the positive and negative signals of the charge displacement curve represented electron accumulation and depletion, respectively. The In_2O_3–CeO_x heterostructure displayed a significant charge rearrangement around the crystalline–amorphous heterostructure interface, and electron transfer took place from In_2O_3 to CeO_x, which was in good agreement with the XPS results. Moreover, the reaction pathways for the generation of formate were considered. According to the calculations, the Gibbs free energy for the rate-determining step (RDS) on In_2O_3–CeO_x is lower than that on In_2O_3–CeO_2 and In_2O_3 for the CO_2-to-formate

process (Fig. 5b), suggesting that In_2O_3–CeO_x was thermodynamically more favourable for CO_2-to-formate conversion. The adsorption energies of the *OCHO intermediates on In_2O_3–CeO_x and In_2O_3–CeO_2 were further explained by the projected density of states (p-DOS). As shown in Fig. 5c, the centre of the p-band for In_2O_3–CeO_x–*OCHO was closer to the Fermi level compared with that of In_2O_3–CeO_2–*OCHO, which verified that the antibonding state filling of the In-5p orbital of In_2O_3–CeO_x is lower than that of In_2O_3–CeO_2, thereby enhancing the adsorption strength of *OCHO.[14] In addition, the Gibbs free energy for the dominant competitive HER was also explored (Fig. 5d). The Gibbs free energy for generating *H over In_2O_3–CeO_x was much larger than that for In_2O_3–CeO_2 and In_2O_3, indicating that the HER was more difficult to occur on In_2O_3–CeO_x. Therefore, the crystalline–amorphous In_2O_3–CeO_x heterostructure accelerated the electron transfer, enhanced the adsorption to *OCHO, lowered the energy barrier for the process from OCHO* to *HCOOH, and finally promoted the formation of the formate product. Furthermore, the In_2O_3–CeO_x catalyst significantly suppressed the HER competition reaction compared with In_2O_3 and In_2O_3–CeO_2.

Conclusion

In conclusion, we described a facile strategy to fabricate the crystalline–amorphous In_2O_3–CeO_x heterostructure and studied its performance for the CO_2RR. The experimental results showed that In_2O_3–CeO_x achieved better catalytic performance than the crystalline–crystalline In_2O_3–CeO_2 heterostructure and In_2O_3 alone. The maximum FE of 94.8% was achieved on the In_2O_3–CeO_x catalyst, and the FE remained above 90% over a wide potential range of −0.8 to −1.2 V *vs.* RHE. Detailed studies have shown that there was a remarkable electron transfer from In_2O_3 to amorphous CeO_x on the In_2O_3–

This journal is © the Partner Organisations 2022

Inorg. Chem. Front., 2022, **9**, 5926–5931 | **5929**

CeO_x heterostructure compared to the crystalline–crystalline In_2O_3–CeO_2 heterostructure, which decreased the interfacial charge transfer resistance. The In_2O_3–CeO_x heterostructure promoted the adsorption for *OCHO intermediates and thereby the energy barrier of *OCHO → *HCOOH was reduced, which led to the high selectivity of the CO_2RR to formate. We believe that the work may provide an effective strategy for catalysing CO_2 conversion.

Conflicts of interest

There are no conflicts to declare.

Acknowledgements

Notes and references

1 Y. Y. Birdja, E. Pérez-Gallent, M. C. Figueiredo, A. J. Göttle, F. Calle-Vallejo and M. T. M. Koper, Advances and challenges in understanding the electrocatalytic conversion of carbon dioxide to fuels, *Nat. Energy*, 2019, **4**, 732–745.

2 C. Chen, X. Sun, X. Yan, Y. Wu, H. Liu, Q. Zhu, B. B. A. Bediako and B. Han, Boosting CO_2 electroreduction on N,P-Co-doped carbon aerogels, *Angew. Chem., Int. Ed.*, 2020, **59**, 11123–11129.

3 W. Guo, X. Tan, J. Bi, L. Xu, D. Yang, C. Chen, Q. Zhu, J. Ma, A. Tayal, J. Ma, Y. Huang, X. Sun, S. Liu and B. Han, Atomic indium catalysts for switching CO_2 electroreduction products from formate to CO, *J. Am. Chem. Soc.*, 2021, **143**, 6877–6885.

4 Z. Wang, Y. Zhou, C. Xia, W. Guo, B. You and B. Y. Xia, Efficient electroconversion of carbon dioxide to formate by a reconstructed amino-functionalized indium-organic framework electrocatalyst, *Angew. Chem., Int. Ed.*, 2021, **60**, 19107–19112.

5 N. Han, P. Ding, L. He, Y. Li and Y. Li, Promises of main group metal-based nanostructured materials for electrochemical CO_2 reduction to formate, *Adv. Energy Mater.*, 2020, **10**, 1902338.

6 F. Valentini, V. Kozell, C. Petrucci, A. Marrocchi, Y. Gu, D. Gelman and L. Vaccaro, Formic acid, a biomass-derived source of energy and hydrogen for biomass upgrading, *Energy Environ. Sci.*, 2019, **12**, 2646–2664.

7 W. Guo, S. Liu, X. Tan, R. Wu, X. Yan, C. Chen, Q. Zhu, L. Zheng, J. Ma, J. Zhang, Y. Huang, X. Sun and B. Han, Highly efficient CO_2 electroreduction to methanol through

8 L. Lu, W. Guo, C. Chen, Q. Zhu, J. Ma, H. Wu, D. Yang, G. Yang, X. Sun and B. Han, Synthesis of Sn_4P_3/reduced graphene oxide nanocomposites as highly efficient electrocatalysts for CO_2 reduction, *Green Chem.*, 2020, **22**, 6804–6808.

9 D. Yang, Q. Zhu, X. Sun, C. Chen, W. Guo, G. Yang and B. Han, Electrosynthesis of a defective indium selenide with 3D structure on a substrate for tunable CO_2 electroreduction to syngas, *Angew. Chem., Int. Ed.*, 2020, **59**, 2354–2359.

10 J. E. Pander, M. F. Baruch and A. B. Bocarsly, Probing the mechanism of aqueous CO_2 reduction on post-transition-metal electrodes using ATR-IR spectroelectrochemistry, *ACS Catal.*, 2016, **6**, 7824–7833.

11 J. Li, M. Zhu and Y.-F. Han, Recent advances in electrochemical CO_2 reduction on indium-based catalysts, *ChemCatChem*, 2021, **13**, 514–531.

12 Y. Huang, X. Mao, G. Yuan, D. Zhang, B. Pan, J. Deng, Y. Shi, N. Han, C. Li, L. Zhang, L. Wang, L. He, Y. Li and Y. Li, Size-dependent selectivity of electrochemical CO_2 reduction on converted In_2O_3 nanocrystals, *Angew. Chem., Int. Ed.*, 2021, **60**, 15844–15848.

13 J. Zhang, R. Yin, Q. Shao, T. Zhu and X. Huang, Oxygen vacancies in amorphous InO_x nanoribbons enhance CO_2 adsorption and activation for CO_2 electroreduction, *Angew. Chem., Int. Ed.*, 2019, **58**, 5609–5613.

14 Z. Chen, G. Yu, B. Li, X. Zhang, M. Jiao, N. Wang, X. Zhang and L. Liu, In situ carbon encapsulation confined nickel-doped indium oxide nanocrystals for boosting CO_2 electroreduction to the industrial level, *ACS Catal.*, 2021, **11**, 14596–14604.

15 W. Luo, W. Xie, R. Mutschler, E. Oveisi, G. L. De Gregorio, R. Buonsanti and A. Züttel, Selective and stable electroreduction of CO_2 to CO at the copper/indium interface, *ACS Catal.*, 2018, **8**, 6571–6581.

16 M. A. Ahsan, T. He, J. C. Noveron, K. Reuter, A. R. Puente-Santiago and R. Luque, Low-dimensional heterostructures for advanced electrocatalysis: an experimental and computational perspective, *Chem. Soc. Rev.*, 2022, **51**, 812–828.

17 P. Prabhu, V. Jose and J.-M. Lee, Heterostructured catalysts for electrocatalytic and photocatalytic carbon dioxide reduction, *Adv. Funct. Mater.*, 2020, **30**, 1910768.

18 A. Vasileff, C. Xu, Y. Jiao, Y. Zheng and S.-Z. Qiao, Surface and interface engineering in copper-based bimetallic materials for selective CO_2 electroreduction, *Chem*, 2018, **4**, 1809–1831.

19 P.-F. Sui, C. Xu, M.-N. Zhu, S. Liu, Q. Liu and J.-L. Luo, Interface-induced electrocatalytic enhancement of CO_2-to-formate conversion on heterostructured bismuth-based catalysts, *Small*, 2022, **18**, 2105682.

20 Z. Zhang, F. Ahmad, W. Zhao, W. Yan, W. Zhang, H. Huang, C. Ma and J. Zeng, Enhanced electrocatalytic reduction of CO_2 via chemical coupling between indium

5930 | *Inorg. Chem. Front.*, 2022, **9**, 5926–5931

This journal is © the Partner Organisations 2022

oxide and reduced graphene oxide, *Nano Lett.*, 2019, **19**, 4029–4034.

21 J. Wang, X. Xiao, Y. Liu, K. Pan, H. Pang and S. Wei, The application of CeO_2-based materials in electrocatalysis, *J. Mater. Chem. A*, 2019, **7**, 17675–17702.

22 D. Gao, Y. Zhang, Z. Zhou, F. Cai, X. Zhao, W. Huang, Y. Li, J. Zhu, P. Liu, F. Yang, G. Wang and X. Bao, Enhancing CO_2 electroreduction with the metal–oxide interface, *J. Am. Chem. Soc.*, 2017, **139**, 5652–5655.

23 H. Dong, L. Zhang, L. Li, W. Deng, C. Hu, Z.-J. Zhao and J. Gong, Abundant Ce^{3+} ions in $Au-CeO_x$ nanosheets to enhance CO_2 electroreduction performance, *Small*, 2019, **15**, 1900289.

24 S. Shen, Z. Wang, Z. Lin, K. Song, Q. Zhang, F. Meng, L. Gu and W. Zhong, Crystalline-amorphous interfaces coupling of $CoSe_2$/CoP with optimized d-band center and boosted electrocatalytic hydrogen evolution, *Adv. Mater.*, 2022, **34**, 2110631.

25 M. Yang, M. Zhao, J. Yuan, J. Luo, J. Zhang, Z. Lu, D. Chen, X. Fu, L. Wang and C. Liu, Oxygen vacancies and interface engineering on amorphous/crystalline CrO_x-Ni_3N heterostructures toward high-durability and kinetically accelerated water splitting, *Small*, 2022, **18**, 2106554.

26 Y. X. Duan, Y. T. Zhou, Z. Yu, D. X. Liu, Z. Wen, J. M. Yan and Q. Jiang, Boosting Production of HCOOH from CO_2 Electroreduction via Bi/CeO_x, *Angew. Chem., Int. Ed.*, 2021, **60**, 8798–8802.

27 Z. M. Detweiler, J. L. White, S. L. Bernasek and A. B. Bocarsly, Anodized indium metal electrodes for enhanced carbon dioxide reduction in aqueous electrolyte, *Langmuir*, 2014, **30**, 7593–7600.

28 F. Yang, X. Bao, P. Li, X. Wang, G. Cheng, S. Chen and W. Luo, Boosting hydrogen oxidation activity of Ni in alkaline media through oxygen-vacancy-Rich CeO_2/Ni heterostructures, *Angew. Chem., Int. Ed.*, 2019, **58**, 14179–14183.

29 Y. Wang, W. Zhou, R. Jia, Y. Yu and B. Zhang, Unveiling the activity origin of a copper-based electrocatalyst for selective nitrate reduction to ammonia, *Angew. Chem., Int. Ed.*, 2020, **59**, 5350–5354.

30 C. Zhang, Y. Huang, Y. Yu, J. Zhang, S. Zhuo and B. Zhang, Sub-1.1 nm ultrathin porous CoP nanosheets with dominant reactive {200} facets: a high mass activity and efficient electrocatalyst for the hydrogen evolution reaction, *Chem. Sci.*, 2017, **8**, 2769–2775.

31 G. Ciancaleoni, F. Nunzi and L. Belpassi, Charge displacement analysis-A tool to theoretically characterize the charge transfer contribution of halogen bonds, *Molecules*, 2020, **25**, 300–316.

32 Y. Zhou, Y. Yao, R. Zhao, X. Wang, Z. Fu, D. Wang, H. Wang, L. Zhao, W. Ni, Z. Yang and Y. M. Yan, Stabilization of Cu^+ *via* strong electronic interaction for selective and stable CO_2 electroreduction, *Angew. Chem., Int. Ed.*, 2022, **61**, e202205832.

33 D. Sorbelli, E. Rossi, R. W. A. Havenith, J. Klein, L. Belpassi and P. Belanzoni, Gold-aluminyl and gold-diarylboryl complexes: bonding and reactivity with carbon dioxide, *Inorg. Chem.*, 2022, **61**, 7327–7337.